High-Reynolds-number turbulent cavity flow using the lattice Boltzmann method

L. A. Hegele Jr.,[1,2,*] A. Scagliarini,[3,†] M. Sbragaglia,[4,‡] K. K. Mattila,[5,6,§] P. C. Philippi,[7,‖] D. F. Puleri,[1,¶] J. Gounley,[1,#] and A. Randles[1,**]

[1]*Department of Biomedical Engineering, Duke University, Durham, North Carolina 27708, USA*
[2]*Department of Petroleum Engineering, Santa Catarina State University, Balneário Camboriú, Santa Catarina 88336-275, Brazil*
[3]*CNR-IAC, Institute for Applied Mathematics "M. Picone," 00185 Rome, Italy*
[4]*Department of Physics and INFN, University of "Tor Vergata," 00133 Rome, Italy*
[5]*Department of Physics, and Nanoscience Center, University of Jyväskylä, FI-40014 Jyväskylä, Finland*
[6]*Department of Physics, Tampere University of Technology, FI-33101 Tampere, Finland*
[7]*Mechanical Engineering Graduate Program, Pontifical Catholic University of Paraná, Curitiba, Paraná 80215-901, Brazil*

(Received 15 July 2017; revised manuscript received 24 October 2017; published 4 October 2018)

We present a boundary condition scheme for the lattice Boltzmann method that has significantly improved stability for modeling turbulent flows while maintaining excellent parallel scalability. Simulations of a three-dimensional lid-driven cavity flow are found to be stable up to the unprecedented Reynolds number $\mathrm{Re} = 5 \times 10^4$ for this setup. Excellent agreement with energy balance equations, computational and experimental results are shown. We quantify rises in the production of turbulence and turbulent drag, and determine peak locations of turbulent production.

DOI: 10.1103/PhysRevE.98.043302

I. INTRODUCTION

Fluid dynamic turbulence is a fundamental problem for theoretical physics and applied engineering [1,2]. Particularly complex, yet paramount for a *plethora* of real-life situations (both of natural and technological relevance), is the case of wall-bounded turbulence. Here, in general, one has to cope with statistically nonhomogeneous and anisotropic flows, where highly nontrivial interactions between bulk and boundary layer physics emerge. Fluids at high Reynolds numbers (Re) inside cavities are paradigmatic of wall-bounded flows and have proven extremely challenging for numerical simulations [3,4]. In addition to being a prototypical case study to test the effectiveness of numerical methods to handle boundary conditions, cavity flows are of interest for a number of applications in different natural and technological contexts: from the mixing of composite materials [5,6] to aneurysms in blood flows [7]. In all such circumstances, a central question is to understand the emergence of flow structures and their topology when Re increases. Unlike other relevant paradigmatic examples of bounded flows, such as the drag crisis of a flow past an obstacle, channel flows, Rayleigh-Bénard convection, and Taylor-Couette flows, high-Reynolds-number lid-driven cavity flows have been so far overlooked as a physics problem. The aim of our paper is, therefore, twofold. On one hand we will introduce a new way of implementing boundary conditions in a regularized lattice Boltzmann method (LBM) and on the other we will provide hints that, at increasing Re, complex flow dynamics emerge in a lid-driven cavity. We study numerically the three-dimensional (3D) lid-driven cavity problem (see Fig. 1), exploring regimes up to the unprecedented Reynolds number of $\mathrm{Re} = 5 \times 10^4$ for this type of flow.

Experimental results are available up to $\mathrm{Re} \equiv u_L L/\nu = 10^4$, where u_L, L, and ν are characteristic velocity, length, and viscosity, respectively, and they have been used to validate and compare to computational methods for the past 30 years [6,8]. With the increasing ubiquity of simulation technologies, the field of turbulent flow hydrodynamics commonly uses computational methods to push the frontier. Direct numerical simulations (DNS) have been conducted with highly accurate Chebyshev collocation methods [9] and have been extended up to Reynolds number $\mathrm{Re} = 2.2 \times 10^4$ [10]. Subgrid scale (SGS) large-eddy simulation (LES) methods have been used to simulate up to $\mathrm{Re} = 1.2 \times 10^4$ [11] and $\mathrm{Re} = 2.2 \times 10^4$ [12].

An alternative approach to computationally solve three-dimensional lid-driven cavity flow is to use lattice Boltzmann methods coupled with SGS turbulence models to simulate flows up to $\mathrm{Re} = 1.2 \times 10^4$ [13,14]. Lattice Boltzmann methods for lid-driven cavity flow have previously used simple boundary conditions, such as bounce-back for the Dirichlet condition at the stationary cavity walls and interpolation schemes [14–16], as well as regularized schemes to improve stability [17]. This improvement in stability for LBM is a key issue, since the time complexity is on the order of L^4.

The previous approaches have never been extended past $\mathrm{Re} = 22\,000$. Given these limitations, both on the computational and the experimental sides, we present a DNS scheme

*luiz.hegele@duke.edu
†a.scagliarini@iac.cnr.it
‡sbragaglia@roma2.infn.it
§keijo.mattila@jyu.fi
‖paulo.philippi@pucpr.br
¶daniel.puleri@duke.edu
#john.gounley@duke.edu
**amanda.randles@duke.edu

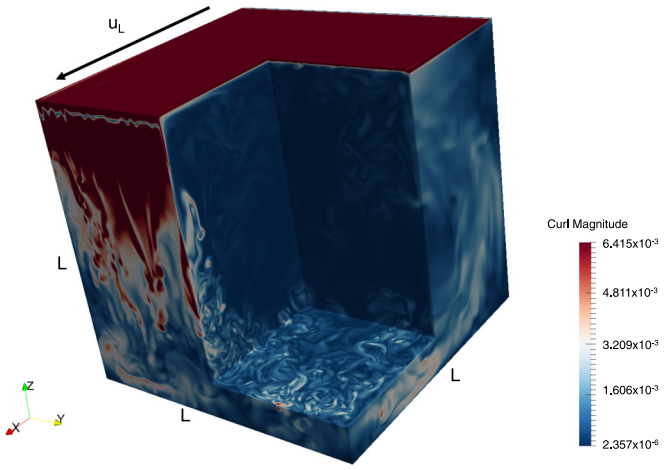

FIG. 1. The magnitude of the vorticity field for the lid-driven cavity flow at $\mathrm{Re} = 4.5 \times 10^4$ and simulation time of $t_{\mathrm{LB}} = 3.3 \times 10^6$ time steps or, in nondimensional units, $t_{\mathrm{ND}} = t_{\mathrm{LB}} u_L / L = 196$. An illustration of the axes and the imposed velocity is also shown. $L = 1024$. Note that the walls have been excluded.

using the regularized lattice Boltzmann method where we introduce a onsite Dirichlet boundary condition, yielding improved stability up to $\mathrm{Re} = 5 \times 10^4$. Due to these improvements, we pave the way to more stable high-Reynolds-number simulations in arbitrary geometries. This LBM framework presents two significant advantages over existing methods. First, the robust stability of the scheme allows simulations to be conducted at lower grid resolutions, without resorting to local mesh refinement or turbulence models. Second, the inherent scalability of both LBM and the boundary conditions leads to a computational model that scales efficiently on high-performance computing resources [18].

II. METHODS

The LBM [19–21] is a discrete kinetic model governed by the following evolution equation for the particle distribution function f:

$$f_i(\boldsymbol{r} + \boldsymbol{c}_i, t+1) = f_i^{(\mathrm{eq})}(\boldsymbol{r}, t) + (1 - \tau^{-1}) \hat{f}_i^{(\mathrm{neq})}(\boldsymbol{r}, t), \quad (1)$$

where $\boldsymbol{r}$, $\boldsymbol{c}_i$, and t are, respectively, the space, microscopic velocity, and time, all in dimensionless units [22,23]. We use the D3Q19 stencil with velocity links $\boldsymbol{c}_i$, $i = 0, \ldots, 18$. We employ the scheme which regularizes f according to the density, momentum, and second-order moments [24,25],

$$\left\{\rho, \rho u_\alpha, \rho m_{\alpha\beta}^{(2)}\right\} = \sum_i g_i \left\{1, c_{i\alpha}, c_{i\alpha} c_{i\beta} - \delta_{\alpha\beta}/a_s^2\right\}, \quad (2)$$

where $\delta_{\alpha\beta}$ is the Kronecker delta, $a_s = \sqrt{3}$ is a scaling factor, and $g_i = f_i$ or $\hat{f}_i$; $\hat{f}$ represents the regularized distribution. The moments in Eq. (2) are generated by the Hermite polynomials of order n denoted by $\mathcal{H}^{(n)}_{\alpha_1 \ldots \alpha_n}$ [26]. The equilibrium function $f^{(\mathrm{eq})}$ is taken as a second-order velocity expansion in the Hermite polynomials:

$$f_i^{(\mathrm{eq})}(\boldsymbol{r}, t) = \rho w_i \left(1 + a_s^2 u_\alpha c_{i\alpha} + \tfrac{1}{2} a_s^4 u_\alpha u_\beta \mathcal{H}^{(2)}_{\alpha\beta,i}\right); \quad (3)$$

w_i are the quadrature weights which depend on the absolute value of the direction $\boldsymbol{c}_i$ (see Appendix A). The second-order moments are projected into the velocity space via

$$\hat{f}_i^{(\mathrm{neq})}(\boldsymbol{r}, t) = \tfrac{1}{2} \rho w_i a_s^4 \left[m_{\alpha\beta}^{(2)} - u_\alpha u_\beta\right] \mathcal{H}^{(2)}_{\alpha\beta,i}. \quad (4)$$

The regularization procedure is completed by

$$\hat{f}_i(\boldsymbol{r}, t) = f_i^{(\mathrm{eq})}(\boldsymbol{r}, t) + \hat{f}_i^{(\mathrm{neq})}(\boldsymbol{r}, t). \quad (5)$$

While the regularization scheme leads to improved general stability of LBM [17,25,27], it does not directly address boundary conditions. Many onsite boundary conditions solve for the unknown distributions using methods such as (i) bounce-back of the nonequilibrium distribution [28]; (ii) iterative scheme to solve for an unknown slip velocity [29]; (iii) diffusive boundary, which assumes that the outgoing stream of particles lose its memory about the incoming stream of particles [30]; or (iv) schemes that replaces only the subset of distributions which are unknown at the boundary [31,32]. However, the restriction to replacing a subset of the distributions leads to instability at even moderate Reynolds numbers [33]. Dorschner *et al.* [34] use a first-order finite-difference scheme to evaluate the second-order moments, related to the strain rate tensor, while the velocities are taken from the previous time step. Krithivasan *et al.* [35] use a combination of the bounce-back rule and the nonlocal diffusive boundary condition. Regularized onsite boundary conditions, which replace the entire distribution at the boundary, have been developed, but encounter instability at large Re and require complex iterative schemes to address edges and corners [33,36]. Alternative approaches involve extrapolation schemes and finite-difference methods to handle flows at large Re, but these methods compromise the inherent parallelism of LBM [37].

Instead, we present a new onsite, Dirichlet-type, regularized boundary condition that uses the second-order moments to solve a system of equations analytically. As the system of equations depends only on lattice topology, this regularized boundary condition applies equally to faces, edges, and corners. In this way, it avoids the usage of iterative solvers (e.g., Refs. [29,36]) or the nonlocality of extrapolation schemes but nonetheless demonstrates robust stability.

Two sets of directions must be defined at the boundary nodes to utilize the current boundary conditions: the incoming to the site particles $I_s = \{i \mid \boldsymbol{r} - \boldsymbol{c}_i \text{ is a fluid site}\}$, and the outgoing from the site particles $O_s = \{j \mid \boldsymbol{c}_j = -\boldsymbol{c}_i, i \in I_s\}$ (see Appendix A for details). At each boundary node—which can be viewed as a fluid node with a distinctive rule of evolution—we compute the quantity

$$\sum_{i \in I_s} f_i \mathcal{H}^{(2)}_{\alpha\beta,i}.$$

The reconstruction process of the distribution function $\hat{f}$ at a boundary node is performed summing the still-unknown regularized particles to obtain the second-order moment as:

$$\sum_{i \in I_s} f_i \mathcal{H}^{(2)}_{\alpha\beta,i} + \sum_{i \notin I_s} \hat{f}_i \mathcal{H}^{(2)}_{\alpha\beta,i} = \rho m_{\alpha\beta}^{(2)}. \quad (6)$$

The second-order moment $\rho m^{(2)}_{\alpha\beta}$ can be decomposed as a sum of regularized particle distributions,

$$\rho m^{(2)}_{\alpha\beta} = \sum_{i\in I_s} \hat{f}_i \mathcal{H}_{\alpha\beta,i}{}^{(2)} + \sum_{i\notin I_s} \hat{f}_i \mathcal{H}_{\alpha\beta,i}{}^{(2)}.$$

The decomposition above combined with Eq. (6) leads to the following set of $D(D+1)/2$ equations (D is the Euclidean dimension):

$$\sum_{i\in I_s} f_i \mathcal{H}_{\alpha\beta,i}{}^{(2)} = \sum_{i\in I_s} \hat{f}_i \mathcal{H}_{\alpha\beta,i}{}^{(2)}. \tag{7}$$

Since we are dealing with Dirichlet boundary conditions, the velocity $\boldsymbol{u}$ is known *a priori*. As a closure relation, we impose the mass conservation during the collision process at the boundary node:

$$\begin{aligned}\sum_{i\in I_s} f_i(\boldsymbol{r},t) &= \sum_{i\in O_s} f_i(\boldsymbol{r}+\boldsymbol{c}_i, t+1)\\ &= (1-\tau^{-1})\sum_{i\in O_s}\hat{f}_i(\boldsymbol{r},t) + \tau^{-1}\sum_{i\in O_s} f_i^{(\mathrm{eq})}(\boldsymbol{r},t),\end{aligned} \tag{8}$$

where we have used an equivalent form of Eq. (1):

$$f_i(\boldsymbol{r}+\boldsymbol{c}_i, t+1) = (1-\tau^{-1})\hat{f}_i(\boldsymbol{r},t) + \tau^{-1} f_i^{(\mathrm{eq})}(\boldsymbol{r},t).$$

The relation expressed in Eq. (8) means that the number of incoming particles to the site, represented in the left-hand side, is *exactly* equal to the number of outgoing particles from the site, represented by the right-hand side. The solution of the system of Eqs. (7) and (8) for the unknowns ρ and $m^{(2)}_{\alpha\beta}$ makes possible the projection of the particle distribution function through Eq. (5), since $\hat{f}$ is a function of ρ, u_α, and $m^{(2)}_{\alpha\beta}$, only, and the particle distribution function is then explicitly written, using Eq. (5), as:

$$\hat{f}_i(\boldsymbol{r},t) = \rho w_i\left(1 + a_s^2 u_\alpha c_{i\alpha} + \tfrac{1}{2}a_s^4 m^{(2)}_{\alpha\beta}\mathcal{H}^{(2)}_{\alpha\beta,i}\right). \tag{9}$$

It follows that the system of equations composed by Eqs. (7) and (8) has analytical solutions for all kinds of neighborhoods: faces, edges, and corners. General forms of Eqs. (7) and (8), as well as explicit relations for the solutions of the above equations, are given in Appendix A.

III. RESULTS

The flow occurs in a cubic cavity driven by a constant tangential velocity equal to $\boldsymbol{u} = (u_L, 0, 0)$ applied at the top of the cubic cavity; on the other five faces of the cavity we set the velocity to zero. We compare our method to the work of Montessori *et al.* [17], who have implemented a regularized LB using the boundary condition described in Guo *et al.* [38] and also a plain BGK version of the LBM, without regularization. It can be seen in Fig. 2 that our proposed method greatly enhances stability, generally using only 60% of the grid points for the other best-case scenario—the regularized LB with the boundary conditions of Guo *et al.* Importantly, the only difference between our scheme and the one used in Ref. [17] is the boundary condition. Due to the time complexity of the fourth order and by reducing the required grid size for a stable simulation, we increase the space of feasible high-resolution simulations.

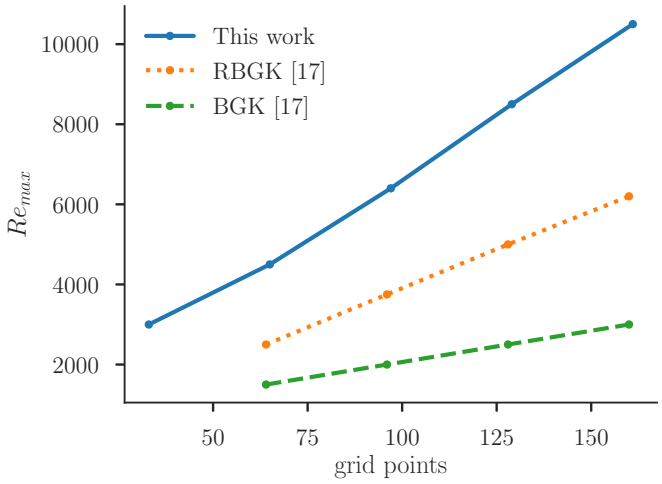

FIG. 2. Plot of the maximum stable Reynolds number for the lid-driven cavity flow *versus* the number of grid points used in several lattice Boltzmann schemes: plain BGK (bottom line), regularized LB (middle line) using Guo *et al.* boundary conditions, and this work (top line). Data from regularized (middle line) and plain BGK (bottom line) were extracted from Ref. [17].

We present results for Re between 10^3 and 5×10^4 and for resolutions of $L = \{256, 511, 1024\}$. We set $u_L = 0.1c_s$, where $c_s = 1/\sqrt{3}$ is the sound speed in the LB fluid, avoiding compressibility effects by keeping the Mach number low. The relaxation time is tuned to set the Reynolds number through the viscosity $\nu = (\tau - 1/2)/a_s^2$. The pressure p is given by $p = c_s^2\rho$.

To validate our code, we compare our results to those of Ref. [9], where highly accurate numerical results for lid-driven cavity simulations using spectral methods are presented. The comparison is favorable, with no discernible differences between the two $\mathrm{Re} = 10^3$ results for both velocity and pressure. A plot of the two sets of traces can be seen in in Fig. 3.

To further verify the model's consistency, we performed two direct comparisons with theoretical results, deriving exact relations from the total kinetic energy and the turbulent kinetic energy balance equations. These relations act as validation since there are no experimental or computational results to compare with for $\mathrm{Re} = 1.5\times10^4$ and above.

The total kinetic energy, the strain rate tensor, $S_{\alpha\beta} = \frac{1}{2}(\partial_\alpha u_\beta + \partial_\beta u_\alpha)$, and the squared velocity u_x^2, are related in the following way:

$$\langle S^2\rangle_\mathcal{V} = \frac{1}{4L}\partial_z\overline{u_x^2}(z)\big|_{z=L}, \tag{10}$$

where $S^2 \equiv S_{\alpha\beta}S_{\alpha\beta}$. The symbol $\langle ...\rangle_\mathcal{V}$ denotes an average over the whole volume, while $\overline{(\dots)}(z)$ stands for an average over the xy plane; a time average over a statistically stationary state is also implied. Equation (10) expresses the balance between power input from the lid (right-hand side) and dissipation (left-hand side). The strain rate tensor (left-hand side) is locally computed using the expression given in Appendix B, while the right-hand side is evaluated with finite differences.

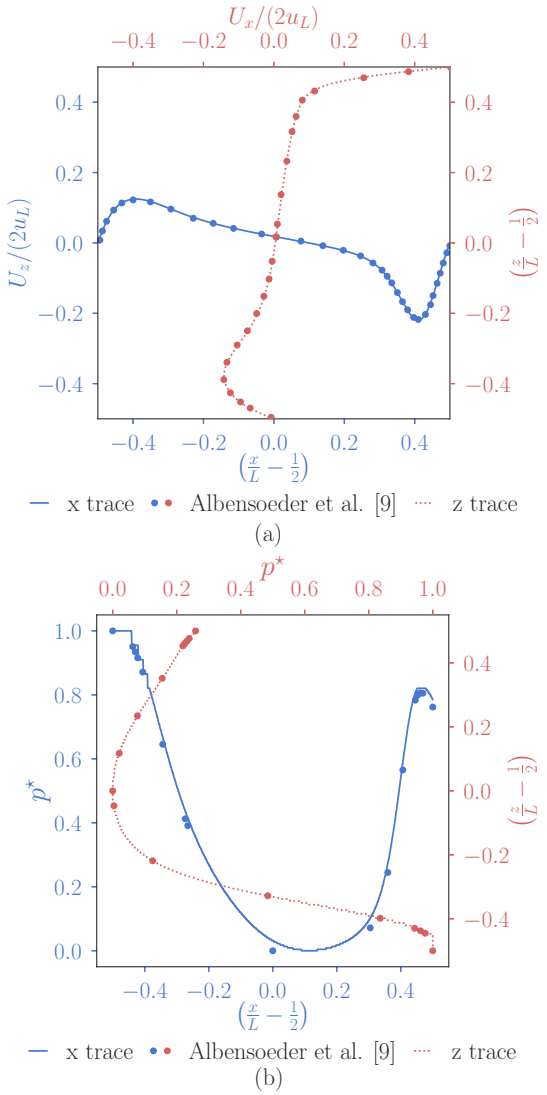

FIG. 3. (a) Plot of normal velocity traces along the centerlines of the x and z. (b) Plot of the normalized pressure traces along the same dimensions. The normalized pressure is defined as: $p^\star = (p - p_{\min})/(p_{\max} - p_{\min})$, where $p_{\min}$ and $p_{\max}$ are the minimum and maximum pressure, respectively, along the centerline. Both plots are for Re $= 10^3(L = 1024)$. The data in circles for each plot were extracted from Ref. [9].

For the turbulent kinetic energy equation, the production $\mathcal{P}$ and the dissipation ϵ of turbulent kinetic energy obey the following relation [39]:

$$\langle \mathcal{P} \rangle_{\mathcal{V}} = \langle \epsilon \rangle_{\mathcal{V}}. \tag{11}$$

Relations (10) and (11) examine the large and small scales, respectively; details of their derivation are shown in Appendix B. Results for the relative errors of the validation ratios $r_S \equiv 4L\langle S^2\rangle_{\mathcal{V}}/\partial_z\overline{u_x^2}(z)|_{z=L}$ and $r_\epsilon \equiv \langle\epsilon\rangle_{\mathcal{V}}/\langle\mathcal{P}\rangle_{\mathcal{V}}$ are shown in Table I. The errors for the runs up to Re $= 5 \times 10^4$ are limited to ∼5% at the large scales and to ∼10% at the small scales. As required by direct numerical numerical simulations, the lattice Boltzmann grid spacing, $\Delta_{\rm LB} = 1$, should be sufficiently small to solve the Kolmogorov scale η

$$\eta = \left(\frac{\nu^3}{\langle\epsilon\rangle_{\mathcal{V}}}\right)^{1/4}. \tag{12}$$

Using Eq. (11) and the nondimensional production of turbulent kinetic energy $\mathcal{P}^\star = \mathcal{P}/(u_L^3/L)$, Eq. (12) is written as

$$\frac{\eta}{L} = \langle\mathcal{P}^\star\rangle_{\mathcal{V}}^{-1/4}\mathrm{Re}^{-3/4}.$$

Taking the extreme case Re $= 5 \times 10^4$ $(L = 1024)$, the calculated production is $\langle\mathcal{P}^\star\rangle_{\mathcal{V}} = 8.32 \times 10^{-4}$ (see Table II), and the corresponding Kolmogorov scale is $\eta = 1.80$, which conforms with the requirement $\Delta_{\rm LB} \leqslant \eta$ [34,40].

In Fig. 4 we present the profiles of $U_x(x = L/2, y = L/2, z)$ along the vertical coordinate for different Reynolds numbers. The mean velocity is given by $\langle u_\alpha\rangle \equiv U_\alpha$, where $\langle ...\rangle$ indicates a temporal average over the stationary state. For the sake of further validation, we compare our numerical data (solid lines) with experimental results from Ref. [8], for Re $= 3.2 \times 10^3$ and Re $= 10^4$, finding very good agreement. We

TABLE I. Relative error values for the validation ratios $r_S = 4L\langle S^2\rangle_{\mathcal{V}}/\partial_z\overline{u_x^2}(z)|_{z=L}$ (a) and $r_\epsilon \equiv \langle\epsilon\rangle_{\mathcal{V}}/\langle\mathcal{P}\rangle_{\mathcal{V}}$ (b). Results are shown for several Reynolds numbers and resolutions. The dash symbols represent numerical unstable solutions.

(a) Relative error in r_S, $\|r_S - 1\|$			
Re	$L = 256$	$L = 511$	$L = 1024$
3.2×10^3	6.9%	3.5%	1.6%
1.0×10^4	10.2%	4.8%	2.6%
1.5×10^4	13.8%	5.6%	2.9%
2.5×10^4	–	8.2%	3.4%
4.0×10^4	–	–	4.8%
4.5×10^4	–	–	5.0%
5.0×10^4	–	–	5.6%
(b) Relative error in r_ϵ, $\|r_\epsilon - 1\|$			
1.0×10^4	9.1%	8.4%	10.5%
1.5×10^4	8.5%	2.2%	6.1%
2.5×10^4	–	5.4%	3.3%
4.0×10^4	–	–	1.7%
4.5×10^4	–	–	2.2%
5.0×10^4	–	–	1.3%

TABLE II. Results for the nondimensional production of turbulent kinetic energy, or production, $\mathcal{P}^\star = \mathcal{P}/(u_L^3/L)$, as a function of the Reynolds number $(L = 1024)$. The following results are shown: the average production over the whole cavity, $\langle\mathcal{P}^\star\rangle_{\mathcal{V}}$; the maximum value for the average of production at the yz plane, $\overline{\mathcal{P}^\star}(x)$; and the location $x^\star_{\max} = x_{\max}/L$ for the peak of production.

Re	$\langle\mathcal{P}^\star\rangle_{\mathcal{V}}$	$\overline{\mathcal{P}^\star}(x^\star_{\max})$	$x^\star_{\max}$
1.0×10^4	3.62×10^{-4}	2.68×10^{-3}	0.966
1.5×10^4	4.23×10^{-4}	3.88×10^{-3}	0.970
2.5×10^4	4.69×10^{-4}	6.42×10^{-3}	0.978
4.0×10^4	7.41×10^{-4}	2.07×10^{-2}	0.989
4.5×10^4	7.77×10^{-4}	2.51×10^{-2}	0.990
5.0×10^4	8.32×10^{-4}	2.85×10^{-2}	0.991

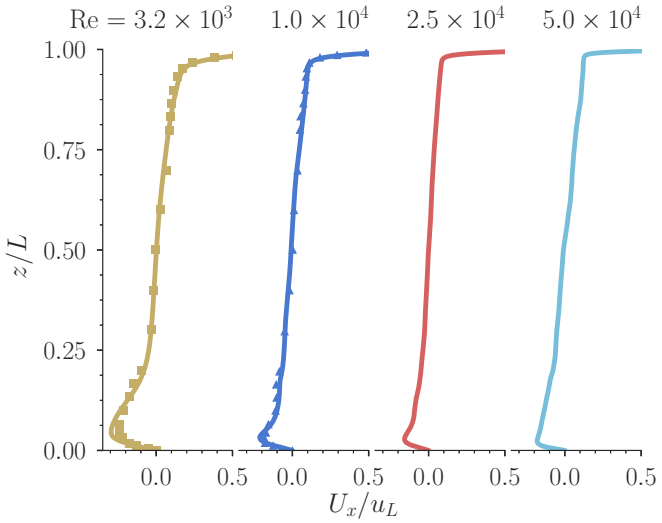

FIG. 4. Normalized averaged velocity profiles in the x direction, U_x/u_L, along the z axis at $x = y = L/2$ for Reynolds numbers $\mathrm{Re} = 3.2 \times 10^3$, 10^4, 2.5×10^4, and 5×10^4 ($L = 1024$). Experimental values for $\mathrm{Re} = 3.2 \times 10^3$ and $\mathrm{Re} = 10^4$ (symbols □ and △) were extracted from Ref. [8].

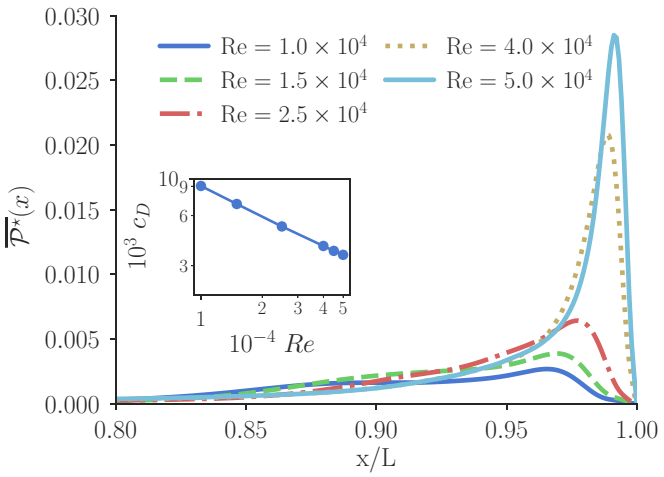

FIG. 5. Average production of the turbulent kinetic energy in the x direction (yz plane), $\overline{\mathcal{P}^\star}(x)$, for Reynolds numbers 10^4, 1.5×10^4, 2.5×10^4, and 4.5×10^4. The resolution is $L = 1024$. Since the values of the mean production for $0 \leqslant x/L \leqslant 0.8$ are $\approx 10^{-4}$ for all Re, only values for $x/L \geqslant 0.8$ are shown. Inset: log-log plot of the turbulent drag coefficient $C_D \equiv 2\nu\langle S^2\rangle L/u_L^3$ versus Reynolds number: Dots are the numerical data, the dashed line corresponds to the scaling $C_D \sim \mathrm{Re}^{-2/3}$.

also show the profiles for $\mathrm{Re} = 2.5 \times 10^4$ and $\mathrm{Re} = 5 \times 10^4$. As seen in Fig. 4, when the Reynolds number increases, there is a decrease in the peak of the minimum of U_x near the bottom wall. This is an effect of the increased production of turbulence: As Re increases, in fact, turbulent fluctuations tend to disrupt the large-scale circulation. Consequently, the drag coefficient, defined as

$$C_D = \frac{2\nu\langle S^2\rangle}{\left(u_L^3/L\right)}, \tag{13}$$

decreases with Re more slowly than in the laminar case, $\sim \mathrm{Re}^{-1}$ (in particular we observe that $C_D \sim \mathrm{Re}^{-2/3}$, see inset of Fig. 5). For $\mathrm{Re} = 5 \times 10^4$, the minimum velocity U_x/u_L is -0.181, and the velocity profile becomes almost flat. Hitherto computational results have not vastly exceeded experimental results so there was no incentive to perform quantitative experiments past $\mathrm{Re} = 10^4$. Given the new results at greater Reynolds number, such as in Fig. 4, we encourage others to further probe this new regime.

Figure 5 shows the profiles of the turbulence production $\overline{\mathcal{P}}(x)$, averaged in yz planes. For all of the production curves there is a peak followed by a fast decay from the downstream wall (plane $x = L$), towards the negative direction of the x axis, until $x \approx 0.8L$, when the production becomes approximately constant. The high peaks of production for $\mathrm{Re} \geqslant 4 \times 10^4$ in the vicinity of the downstream wall indicate a larger conversion of mean (nonturbulent) kinetic energy to turbulent kinetic energy, resulting in turbulent drag. In Table II we present the results for the average production over the whole system, as well as the value of the production peak and the x coordinate where this peak happens. Both the nondimensional average volumetric production $\langle\mathcal{P}^\star\rangle_\mathcal{V}$ and maximum average areal production $\overline{\mathcal{P}^\star}(x)$ increase with the Reynolds number. The location where the maximum production occurs moves closer to the wall, from 4% to 1% of L — indicating that the boundary layer thickness decreases as Re increases from 10^4 to 4.5×10^4. In Fig. 6 we plot the maximum production $\overline{\mathcal{P}^\star}(x^\star_{\mathrm{max}})$ vs. Re: interestingly, we observe a linear relationship $\overline{\mathcal{P}^\star}(x^\star_{\mathrm{max}}) \propto \mathrm{Re}$ for Re up to 2.5×10^4, whereas $\overline{\mathcal{P}^\star}(x^\star_{\mathrm{max}}) \propto \mathrm{Re}^{3/2}$ for $\mathrm{Re} \geqslant 4 \times 10^4$. The latter might be the indication that for some critical Reynolds $2.5 \times 10^4 < \mathrm{Re}_c < 4 \times 10^4$ a transition to a new dynamical regime occurs, characterized by the presence of further topological structures in the flow. This picture is corroborated by Fig. 7, where we plot the probability density function (pdf) of the Laplacian of the pressure field $\Delta p \equiv \partial^2_{\alpha\alpha} p$. The latter fulfills, for an incompressible velocity

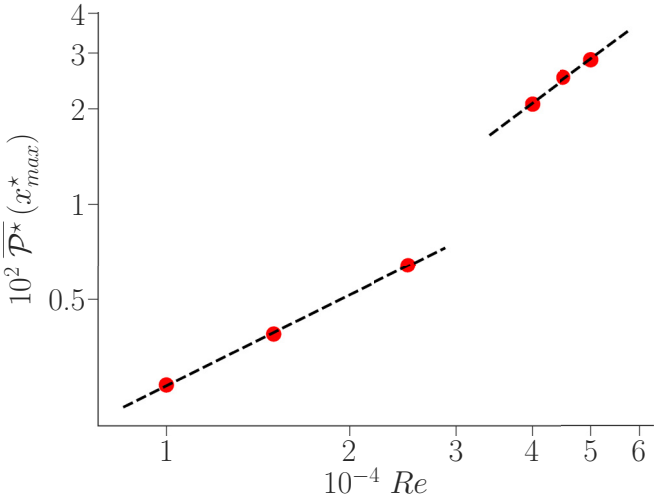

FIG. 6. Maximum production of the turbulent kinetic energy at the yz plane vs. Re. Dashed lines indicate the power laws $\overline{\mathcal{P}^\star}(x^\star_{\mathrm{max}}) \propto \mathrm{Re}$, for $\mathrm{Re} \leqslant 2.5 \times 10^4$, and $\overline{\mathcal{P}^\star}(x^\star_{\mathrm{max}}) \propto \mathrm{Re}^{3/2}$, for $4 \times 10^4 \leqslant \mathrm{Re} \leqslant 5 \times 10^4$.

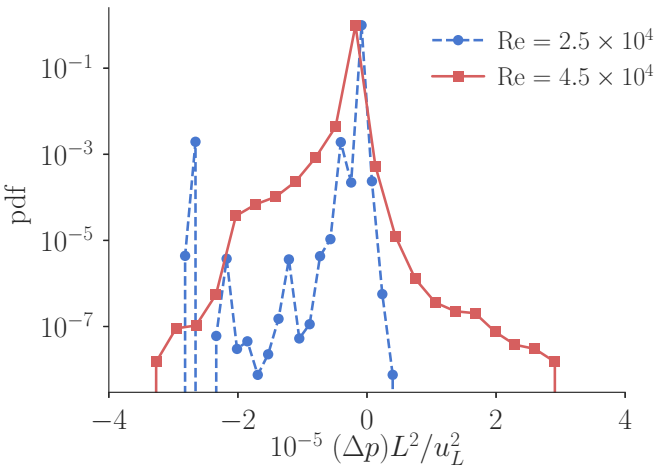

FIG. 7. Probability density function (pdf) of the Laplacian of the pressure field Δp, computed over the whole volume, for Re $= 2.5 \times 10^4$ and Re $= 4.5 \times 10^4$ ($L = 1024$).

field, the following equality:

$$\Delta p = \Omega^2 - S^2, \tag{14}$$

where S^2 is the trace of square strain rate tensor (defined as above), and $\Omega^2 = \Omega_{\alpha\beta}\Omega_{\alpha\beta}$ is the trace of the square of the antisymmetric part of the gradient tensor, $\Omega_{\alpha\beta} = \frac{1}{2}(\partial_\alpha u_\beta - \partial_\beta u_\alpha)$. Minima of the pressure field, where $\Delta p > 0$, correspond to regions of high rotation and low strain, like vortex cores. We observe in Fig. 7 that the pdf of Δp develops a fat tail at large positive values when Re is increased from 2.5×10^4 to 4.5×10^4. This tail suggests the emergence of new strong vortical structures, on top of the primary and secondary vortices (notice that the magnitude of Δp is given in units of $(u_L/L)^2$, which gives a measure of the enstrophy content of the large-scale primary vortex).

IV. CONCLUSIONS

We have proposed a new lattice Boltzmann boundary condition for Dirichlet problems based on a regularized form of the lattice Boltzmann equation. The robust stability of this DNS scheme allows simulations to be conducted without resorting to local mesh refinement or turbulence models and leads to a computational model that scales efficiently on high-performance computing resources. This numerical scheme is applied to a turbulent flow and simulation results are compared with available experimental data for Re $= 3.2 \times 10^3$ and 10^4, showing good agreement. Simulations are conducted up to Re $= 5 \times 10^4$, beyond the limit that was found in the published literature and leads to new insights into the role of the physical mechanisms that are responsible for the production of the turbulent kinetic energy inside the cavity. Particularly, we find that when Re increases, there is an increasing conversion of the main stream kinetic energy into turbulent kinetic energy along the downstream wall, and the effect of the turbulent drag reveals itself in the velocity field. In a future work, we plan to make a more systematic analysis in terms of scaling properties of global quantities, such as dissipation, momentum fluxes, over an extended the range of Re, in order to probe new emerging dynamical regimes. As a method developed within the lattice Boltzmann framework, it may be directly applied to this class of models. The immediate follow-ups are other standard velocity stencils (like $D3Q27$, $D2Q9$ [41]) and high-order models [42]. For the standard $D3Q27$ and $D2Q9$ velocity sets using BGK, the set of Eqs. (7) and (8) must be solved again and these solutions will give rise to the Dirichlet boundary conditions for these models. Regarding the $D3Q15$ velocity set, there will be no solution for corners, since the number of particle distributions (four) is smaller than the number of equations (seven) leading to an undetermined system, and then the application of the present method is not straightforward for the $D3Q15$. The present model can also be applied to other collision kernels, like the entropic LB [43,44] and the regularized LB with recurrence relations [45,46]. For instance, the present method can be applied to the entropic collision model at the boundaries leading to a nonlinear system of equations in order to guarantee the nonlinear stability of the entropic scheme and the conservation of mass.

ACKNOWLEDGMENTS

Authors thank Cindy Ouyang for helping to write the parallelized version of the code and Gregory Herschlag and Ismael Perez for fruitful discussions. We also thank Volker W. Blum and Erik W. Draeger for a careful reading of the manuscript and insightful suggestions. Research reported in this publication was supported by the Office of the Director, National Institutes of Health of the National Institutes of Health, under Award No. DP5OD019876. This work is also supported by NIH Grant No. T32-EB001040. The content is solely the responsibility of the authors and does not necessarily represent the official views of the National Institutes of Health. Computing support for this work came from the Lawrence Livermore National Laboratory (LLNL) Institutional Computing Grand Challenge program.

APPENDIX A: BOUNDARY CONDITIONS

We provide details of the proposed method for the boundary conditions in the following order: (1) the D3Q19 velocity set; (2) the types of boundary sites: corner, edges, and faces; (3) the explicit equations for the moments; (4) the solutions for all kinds of concave boundary sites; and (5) a summary of the method.

1. D3Q19 stencil

The $D3Q19$ stencil is defined by the following particle dimensionless velocities: $\boldsymbol{c}_0 = (0,0,0)$, $\boldsymbol{c}_1 = (1,0,0)$, $\boldsymbol{c}_2 = (0,1,0)$, $\boldsymbol{c}_3 = (0,0,1)$, $\boldsymbol{c}_4 = (-1,0,0)$, $\boldsymbol{c}_5 = (0,-1,0)$, $\boldsymbol{c}_6 = (0,0,-1)$, $\boldsymbol{c}_7 = (1,1,0)$, $\boldsymbol{c}_8 = (1,0,1)$, $\boldsymbol{c}_9 = (0,1,1)$, $\boldsymbol{c}_{10} = (1,-1,0)$, $\boldsymbol{c}_{11} = (1,0,-1)$, $\boldsymbol{c}_{12} = (-1,1,0)$, $\boldsymbol{c}_{13} = (-1,0,1)$, $\boldsymbol{c}_{14} = (0,1,-1)$, $\boldsymbol{c}_{15} = (0,-1,1)$, $\boldsymbol{c}_{16} = (-1,-1,0)$, $\boldsymbol{c}_{17} = (-1,0,-1)$, $\boldsymbol{c}_{18} = (0,-1,-1)$. The weights w_i associated with the directions $\boldsymbol{c}_i$ are the following: $w_0 = 1/3$; $w_i = 1/18$ for $i = 1,\ldots,6$; and $w_i = 1/36$ for $i = 7,\ldots,18$. An image of the stencil is shown in Fig. 8.

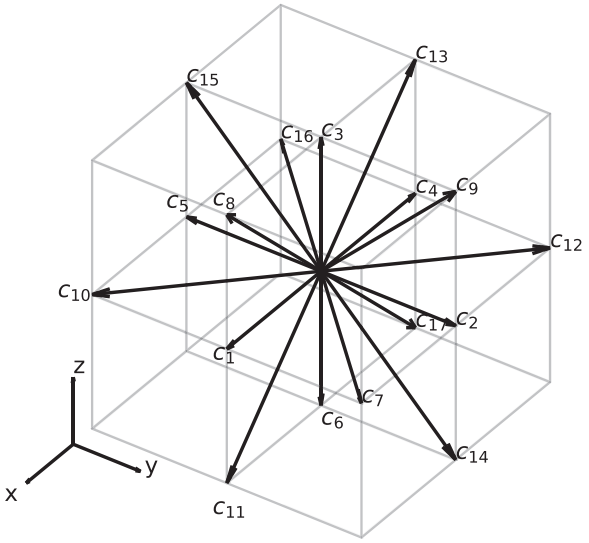

FIG. 8. $D3Q19$ stencil. For simplicity, the origin of the system of coordinates is located at the center of the grid. The velocity vectors of the lattice are shown pointing from the origin toward their next step sites.

2. Boundary sites

In our approach to solve the Dirichlet boundary conditions, we have assumed that the boundaries are aligned with spatial and velocity coordinates, a common practice in lattice Boltzmann (LB). Since we are dealing with a wet-node boundary type, all boundary sites can be divided into three groups: faces, edges, and corners. As mentioned, we have also restricted this work to concave boundaries, considering our main goal was to perform simulations of an LB fluid inside a concave cavity.

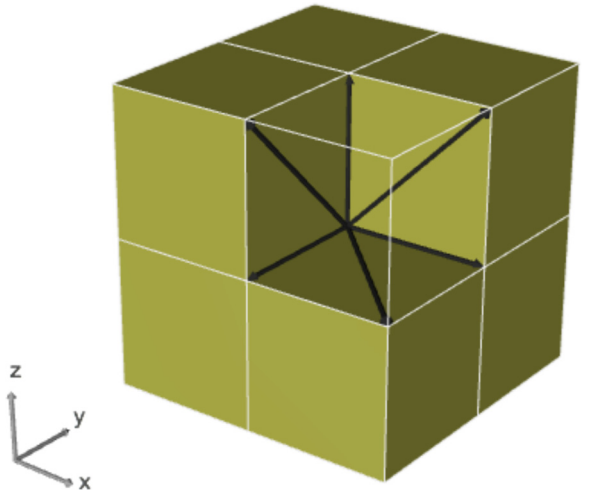

FIG. 9. Example of a corner boundary site, located at the point $(x, y, z) = (0, 0, 0)$. The fluid portion is defined by the intersection of the regions $x \geqslant 0$, $z \geqslant 0$, and $y \leqslant 0$. The normals are given by $\hat{\boldsymbol{n}}_1 = (0, 0, -1)$, $\hat{\boldsymbol{n}}_2 = (-1, 0, 0)$, and $\hat{\boldsymbol{n}}_3 = (0, 1, 0)$. The shaded part of the figure represents the solid region. The visible vectors are the outgoing vectors of a corner boundary site. At this site $l_1 = l_2 = -1$ and $l_3 = 1$. Also, $I = \{0, 2, 4, 6, 12, 14, 17\}$ and $O = \{0, 1, 3, 5, 8, 10, 15\}$.

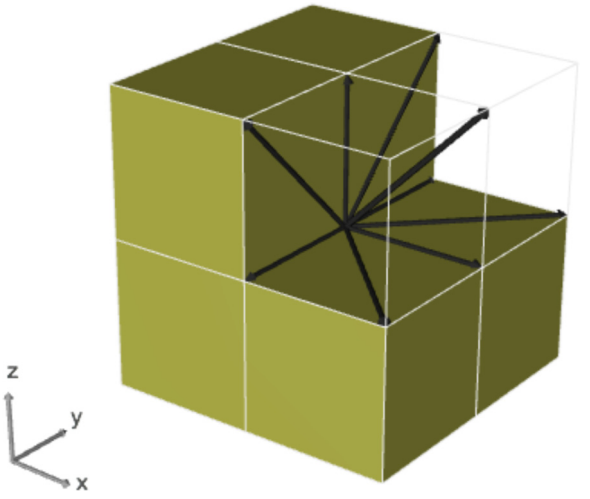

FIG. 10. Example of an edge boundary site, located at the point $(x, y, z) = (0, 0, 0)$. The fluid portion is defined by $z \geqslant 0$ and $x \geqslant 0$. The normals are given by $\hat{\boldsymbol{n}}_1 = (0, 0, -1)$ and $\hat{\boldsymbol{n}}_2 = (-1, 0, 0)$. In this case, $l_1 = l_2 = -1$. The set I is given by $\{0, 2, 4, 5, 6, 12, 14, 16, 17, 18\}$ and the outgoing set is $O = \{0, 1, 2, 3, 5, 7, 8, 9, 10, 15\}$. The visible vectors form the outgoing set at this site.

Nevertheless, we are currently working on the extension of this idea to convex boundary sites as well.

Recall the definitions of the incoming and outgoing directions at a boundary site: The incoming particles to the site index set I_s is defined by $I_s = \{i \mid \boldsymbol{r} - \boldsymbol{c}_i$ is a fluid site$\}$, while the outgoing particles from the site index set O_s is given by $O_s = \{j \mid \boldsymbol{c}_j = -\boldsymbol{c}_i, i \in I_s\}$. Outgoing vectors for a corner, an edge, and a face are shown in Figs. 9, 10, and 11, respectively, while one incoming set of vectors for a face is shown in Fig. 12.

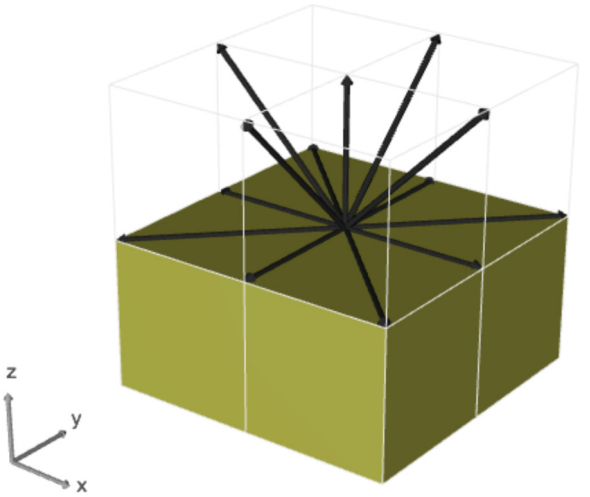

FIG. 11. Example of a face boundary site, located at the point $(x, y, z) = (0, 0, 0)$. The fluid portion is defined by $z \geqslant 0$; the orientation of this face boundary site is defined by the normal $\hat{\boldsymbol{n}}_1 = (0, 0, -1)$ at the xy plane. Also, $l_1 = -1$. The outgoing vectors are shown, and the outgoing set is $O = \{0, 1, 2, 3, 4, 5, 7, 8, 9, 10, 12, 13, 15, 16\}$. The incoming vectors are depicted in Fig. 12.

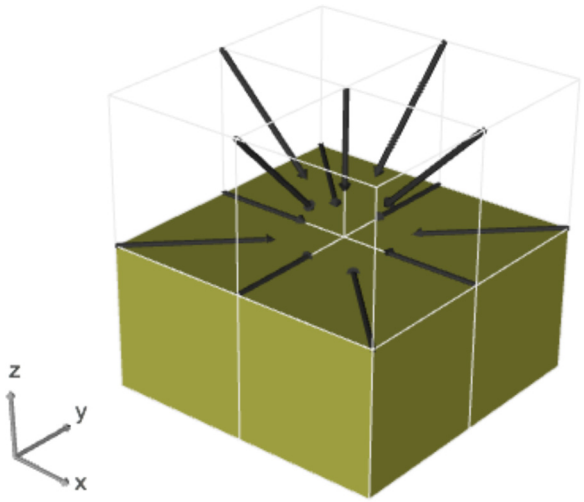

FIG. 12. The same face boundary site of Fig. 11, and now the incoming vectors are shown. With this orientation, the incoming set is given by $I = \{0, 1, 2, 4, 5, 6, 7, 10, 11, 12, 14, 16, 17, 18\}$.

The corner boundary site is defined by the intersection of three perpendicular planes defined by the normals $\hat{\boldsymbol{n}}_k = l_k \hat{\boldsymbol{e}}_k$, where $\hat{\boldsymbol{e}}_k$ is the vector of the canonical basis in $\mathbb{R}^3$ associated with the coordinate x_k. Hereafter, $k = 1, 2, 3$; (x_1, x_2, x_3) is any permutation of the coordinates (x, y, z); and $l_j = \pm 1$ defines the orientation of the planes: the normals must point from the fluid toward the solid (see label in Fig. 9). There are seven incoming and seven outgoing particle distributions at a corner boundary site and a typical one is shown in Fig. 9.

The second type of boundary site is the edge, which is the intersection of two perpendicular planes. The edge is defined by the two normals of these planes, $\hat{\boldsymbol{n}}_1 = l_1 \hat{\boldsymbol{e}}_1$ and $\hat{\boldsymbol{n}}_2 = l_2 \hat{\boldsymbol{e}}_2$. Since there is no need for a third plane, $l_3 = 0$. There are a total of ten elements in the I and O sets, each. An example of an edge is shown if Fig. 10.

The face boundary site is simply defined by a normal vector $\hat{\boldsymbol{n}}_1 = l_1 \hat{\boldsymbol{e}}_1$. In this case, $l_2 = l_3 = 0$. There are 14 incoming—and 14 outgoing—particle distributions at a face boundary site. Figures 11 and 12 depict an example of a face.

3. General explicit equations for the moments

The following known quantities are defined at the boundary sites:

$$\rho_I \equiv \sum_{i \in I_s} f_i, \tag{A1}$$

$$\rho_I m^{(2)}_{\alpha\beta,I} \equiv \sum_{i \in I_s} f_i \mathscr{H}^{(2)}_{\alpha\beta,i}, \tag{A2}$$

where Greek letters represent the spatial coordinates, $\mathscr{H}^{(2)}_{\alpha\beta,i} = c_{i\alpha}c_{i\beta} - \delta_{\alpha\beta}/a_s^2$ is the second-order tensor Hermite polynomial, and $a_s = \sqrt{3}$ is the scaling factor. In some places we will also use the equivalent definition

$$m^{(2)}_{\alpha\beta,I} = \rho_I^{-1} \sum_{i \in I_s} f_i \mathscr{H}^{(2)}_{\alpha\beta,i}.$$

Note that in Eqs. (A1) and (A2) the distributions f_i are the incoming populations, so they are not regularized yet. Now, recall that the system of equations for the moments $m^{(2)}_{\alpha\beta}$ and ρ is given by the following $D(D+1)/2 + 1$ equations:

$$\rho_I m^{(2)}_{\alpha\beta,I} = \sum_{i \in I_s} \hat{f}_i \mathscr{H}^{(2)}_{\alpha\beta,i}, \tag{A3}$$

$$\rho_I = (1-\omega) \sum_{i \in O_s} \hat{f}_i(\boldsymbol{r}, t) + \omega \sum_{i \in O_s} f_i^{(\mathrm{eq})}(\boldsymbol{r}, t), \tag{A4}$$

where $\omega = \tau^{-1}$ and D is the number of spatial dimensions. Equations (A3) and (A4) are Eqs. (7) and (8) from the main text. In three dimensions, for instance, there are seven equations total, and in the following we will proceed with $D = 3$. Due to the Dirichlet-type of boundary conditions, the velocities u_{x_1}, u_{x_2}, and u_{x_3} are prescribed so Eqs. (A3) and (A4) lead to a system of equations for the unknown moments ρ and $m^{(2)}_{\alpha\beta}$, since $\hat{f}$ is a function of ρ, u_α, and $m^{(2)}_{\alpha\beta}$ only.

In order to avoid a nonlinear system of equations, we will now seek solutions for $\rho m^{(2)}_{\alpha\beta}$ instead of $m^{(2)}_{\alpha\beta}$.

We split the set of Eqs. (A3) into their diagonal moments $\rho_I m^{(2)}_{x_1x_1,I}$, $\rho_I m^{(2)}_{x_2x_2,I}$, and $\rho_I m^{(2)}_{x_3x_3,I}$ and the nondiagonal moments $\rho_I m^{(2)}_{x_1x_2,I}$, $\rho_I m^{(2)}_{x_1x_3,I}$, and $\rho_I m^{(2)}_{x_2x_3,I}$. We will make use of a modified δ function, defined by:

$$\tilde{\delta}_{l_k} = \begin{cases} 1, & \text{if } l_k = 0, \\ 0, & \text{otherwise,} \end{cases}$$

valid for $k = 1, 2, 3$.

For the diagonal moment $\rho m^{(2)}_{x_1x_1,I}$, the regularized distribution of the right-hand side in Eq. (A3) is expanded and summed in a general way, taking into account the geometrical parameters that form the boundaries, leading to:

$$\begin{aligned} \rho_I m^{(2)}_{x_1x_1,I} = {} & \rho\left(P^{(1)}_{123} + u_{x_1} P^{(u)}_{123} + u_{x_2} S^{(u)}_{123} + u_{x_3} S^{(u)}_{132}\right) \\ & + \rho m^{(2)}_{x_1x_1} P^{(m)}_{123} + \rho m^{(2)}_{x_2x_2} S^{(m)}_{123} + \rho m^{(2)}_{x_3x_3} S^{(m)}_{132} \\ & + \rho m^{(2)}_{x_1x_2} \tfrac{1}{6} l_1 l_2 + \rho m^{(2)}_{x_1x_3} \tfrac{1}{6} l_1 l_3 - \rho m^{(2)}_{x_2x_3} \tfrac{1}{12} l_2 l_3, \end{aligned} \tag{A5}$$

where we have defined

$$\begin{aligned} P^{(1)}_{pqr} = {} & -\frac{1}{12} + \frac{2}{27}\tilde{\delta}_{l_p} + \frac{1}{54}\tilde{\delta}_{l_p}(\tilde{\delta}_{l_q} + \tilde{\delta}_{l_r}) \\ & - \frac{1}{108}\left(\tilde{\delta}_{l_q} + \tilde{\delta}_{l_r} + \tilde{\delta}_{l_q}\tilde{\delta}_{l_r}\right), \end{aligned} \tag{A6}$$

$$P^{(u)}_{pqr} = l_p\left(\frac{2}{9} + \frac{\tilde{\delta}_{l_q}}{18} + \frac{\tilde{\delta}_{l_r}}{18}\right), \tag{A7}$$

$$S^{(u)}_{pqr} = \left(-\frac{1}{36} - \frac{\tilde{\delta}_{l_r}}{36} + \frac{\tilde{\delta}_{l_p}}{18}\right) l_q, \tag{A8}$$

$$P^{(m)}_{pqr} = \frac{11}{24} + \frac{2}{9}\tilde{\delta}_{l_p} + \frac{7}{72}\left(\tilde{\delta}_{l_q} + \tilde{\delta}_{l_r}\right) + \frac{\tilde{\delta}_{l_p}}{18}\left(\tilde{\delta}_{l_q} + \tilde{\delta}_{l_r}\right) + \frac{1}{72}\tilde{\delta}_{l_q}\tilde{\delta}_{l_r}, \tag{A9}$$

$$\begin{aligned} S^{(m)}_{pqr} = {} & \frac{1}{12} - \frac{1}{36}\left(\tilde{\delta}_{l_p} + \tilde{\delta}_{l_q} + \tilde{\delta}_{l_r}\right) \\ & - \frac{1}{36}\left(\tilde{\delta}_{l_p} + \tilde{\delta}_{l_q}\right)\tilde{\delta}_{l_r} + \frac{1}{18}\tilde{\delta}_{l_p}\tilde{\delta}_{l_q}, \end{aligned} \tag{A10}$$

and $\{p, q, r\}$ can assume all of the permutations of the set $\{1, 2, 3\}$. Equations (A6)–(A10) depend purely on geometrical parameters given by the definition of the boundary. Analogous expressions can be readily written for the other two diagonal terms, $\rho_I m^{(2)}_{x_2x_2,I}$ and $\rho_I m^{(2)}_{x_3x_3,I}$ based on the symmetric properties of the terms in Eq. (A5). These full equations for $\rho_I m^{(2)}_{x_2x_2,I}$ and $\rho_I m^{(2)}_{x_3x_3,I}$ read as follows:

$$\begin{aligned}\rho_I m^{(2)}_{x_2x_2,I} =& \rho\big(P^{(1)}_{213} + u_{x_2}P^{(u)}_{213} + u_{x_1}S^{(u)}_{213} + u_{x_3}S^{(u)}_{231}\big)\\ &+ \rho m^{(2)}_{x_2x_2}P^{(m)}_{213} + \rho m^{(2)}_{x_1x_1}S^{(m)}_{213} + \rho m^{(2)}_{x_3x_3}S^{(m)}_{231}\\ &+ \rho m^{(2)}_{x_1x_2}\tfrac{1}{6}l_1l_2 + \rho m^{(2)}_{x_2x_3}\tfrac{1}{6}l_2l_3 - \rho m^{(2)}_{x_1x_3}\tfrac{1}{12}l_1l_3,\end{aligned} \tag{A11}$$

$$\begin{aligned}\rho_I m^{(2)}_{x_3x_3,I} =& \rho\big(P^{(1)}_{312} + u_{x_3}P^{(u)}_{312} + u_{x_1}S^{(u)}_{312} + u_{x_2}S^{(u)}_{321}\big)\\ &+ \rho m^{(2)}_{x_3x_3}P^{(m)}_{312} + \rho m^{(2)}_{x_1x_1}S^{(m)}_{312} + \rho m^{(2)}_{x_2x_2}S^{(m)}_{321}\\ &+ \rho m^{(2)}_{x_1x_3}\tfrac{1}{6}l_1l_3 + \rho m^{(2)}_{x_2x_3}\tfrac{1}{6}l_2l_3 - \rho m^{(2)}_{x_1x_2}\tfrac{1}{12}l_1l_2.\end{aligned} \tag{A12}$$

For the nondiagonal moment $\rho_I m^{(2)}_{x_1,x_2,I}$ the same argument that we have used to obtain Eq. (A5) is applied and we can extract from Eq. (A3)

$$\begin{aligned}\rho_I m^{(2)}_{x_1x_2,I} =& \rho\big(Q^{(1)}_{12} + u_{x_1}Q^{(u)}_{12} + u_{x_2}Q^{(u)}_{21}\big)\\ &+ \rho m^{(2)}_{x_1x_1}\tfrac{1}{12}l_1l_2 + \rho m^{(2)}_{x_2x_2}\tfrac{1}{12}l_1l_2\\ &- \rho m^{(2)}_{x_3x_3}\tfrac{1}{24}l_1l_2 + \rho m^{(2)}_{x_1x_2}Q^{(m)}_{12},\end{aligned} \tag{A13}$$

where

$$Q^{(1)}_{pq} = \tfrac{1}{36}l_pl_q, \tag{A14}$$

$$Q^{(u)}_{pq} = \tfrac{1}{12}\big(1 + \tilde{\delta}_{l_p}\big)l_q, \tag{A15}$$

$$Q^{(m)}_{pq} = \tfrac{1}{4}\big(1 + \tilde{\delta}_{l_p}\big)\big(1 + \tilde{\delta}_{l_q}\big). \tag{A16}$$

In Eqs. (A14)–(A16), $Q^{(1)}_{pq}$, $Q^{(u)}_{pq}$, and $Q^{(m)}_{pq}$ are dependent only on the geometrical parameters of the boundary site. For the other two nondiagonal terms, namely $\rho_I m^{(2)}_{x_1x_3,I}$ and $\rho_I m^{(2)}_{x_2x_3,I}$, equivalent expressions can be obtained from Eq. (A13) based on symmetry arguments, and for the sake of completeness we write down the full expressions for $\rho_I m^{(2)}_{x_1x_3,I}$ and $\rho_I m^{(2)}_{x_2x_3,I}$:

$$\begin{aligned}\rho_I m^{(2)}_{x_1x_3,I} =& \rho\big(Q^{(1)}_{13} + u_{x_1}Q^{(u)}_{13} + u_{x_3}Q^{(u)}_{31}\big)\\ &+ \rho m^{(2)}_{x_1x_1}\tfrac{1}{12}l_1l_3 + \rho m^{(2)}_{x_3x_3}\tfrac{1}{12}l_1l_3\\ &- \rho m^{(2)}_{x_2x_2}\tfrac{1}{24}l_1l_3 + \rho m^{(2)}_{x_1x_3}Q^{(m)}_{13},\end{aligned} \tag{A17}$$

$$\begin{aligned}\rho_I m^{(2)}_{x_2x_3,I} =& \rho\big(Q^{(1)}_{23} + u_{x_2}Q^{(u)}_{23} + u_{x_3}Q^{(u)}_{32}\big)\\ &+ \rho m^{(2)}_{x_2x_2}\tfrac{1}{12}l_2l_3 + \rho m^{(2)}_{x_3x_3}\tfrac{1}{12}l_2l_3\\ &- \rho m^{(2)}_{x_1x_1}\tfrac{1}{24}l_2l_3 + \rho m^{(2)}_{x_2x_3}Q^{(m)}_{23}.\end{aligned} \tag{A18}$$

Finally, for the mass conservation, the regularized $\hat{f}$ and equilibrium $f^{(\mathrm{eq})}$ particle functions, on the right-hand side of Eq. (A4), are expanded and summed up in the outgoing set index O_s to explicitly obtain:

$$\begin{aligned}\rho_I =& \rho\big(R^{(1)}_{123} + u_{x_1}R^{(u)}_{123} + u_{x_2}R^{(u)}_{231} + u_{x_3}R^{(u)}_{312}\big)\\ &+ \rho\omega\Big(u^2_{x_1}\frac{a_s^4}{2}P^{(1)}_{123} + u^2_{x_2}\frac{a_s^4}{2}P^{(1)}_{231} + u^2_{x_3}\frac{a_s^4}{2}P^{(1)}_{312}\\ &+ u_{x_1}u_{x_2}a_s^4Q^{(1)}_{12} + u_{x_1}u_{x_3}a_s^4Q^{(1)}_{13} + u_{x_2}u_{x_3}a_s^4Q^{(1)}_{23}\Big)\\ &+ (1-\omega)\Big(\rho m^{(2)}_{x_1x_1}\frac{a_s^4}{2}P^{(1)}_{123} + \rho m^{(2)}_{x_2x_2}\frac{a_s^4}{2}P^{(1)}_{231}\\ &+ \rho m^{(2)}_{x_3x_3}\frac{a_s^4}{2}P^{(1)}_{312} + \rho m^{(2)}_{x_1x_2}a_s^4Q^{(1)}_{12}\\ &+ \rho m^{(2)}_{x_1x_3}a_s^4Q^{(1)}_{13} + \rho m^{(2)}_{x_2x_3}a_s^4Q^{(1)}_{23}\Big),\end{aligned} \tag{A19}$$

with

$$R^{(1)}_{pqr} = \tfrac{7}{12} + \tfrac{1}{9}\big(\tilde{\delta}_{l_p} + \tilde{\delta}_{l_q} + \tilde{\delta}_{l_r}\big) + \tfrac{1}{36}\big(\tilde{\delta}_{l_p}\tilde{\delta}_{l_q} + \tilde{\delta}_{l_p}\tilde{\delta}_{l_r} + \tilde{\delta}_{l_q}\tilde{\delta}_{l_r}\big), \tag{A20}$$

$$R^{(u)}_{pqr} = -\tfrac{1}{3}l_p\big(1 + \tfrac{1}{4}(l_q + l_r)\big). \tag{A21}$$

It can readily be seen from Eqs. (A5), (A13), and (A19) that if we set $l_1 = l_2 = l_3 = 0$, i.e., a regular bulk fluid site, the identities $\rho_I = \rho$ and $\rho_I m^{(2)}_{\alpha\beta,I} = \rho m^{(2)}_{\alpha\beta}$ immediately follow.

4. Explicit solution for the boundary conditions

Here we show the solutions for corners, edges, and faces for the system of equations composed by Eqs. (A5), (A13), and (A19).

Corners—A corner is defined by the signs of l_1, l_2, and l_3, and hence $\tilde{\delta}_{l_1} = \tilde{\delta}_{l_2} = \tilde{\delta}_{l_3} = 0$. The solution of the system of equations at the corners is for ρ:

$$\rho = \rho_I\frac{b_C}{d_C}, \tag{A22}$$

where

$$\begin{aligned}b_C =& \tfrac{1}{24}(1-\omega)\big(m^{(2)}_{x_1x_1,I} + m^{(2)}_{x_2x_2,I} + m^{(2)}_{x_3x_3,I}\\ &- 2l_1l_2m^{(2)}_{x_1x_2,I} - 2l_1l_3m^{(2)}_{x_1x_3,I} - 2l_2l_3m^{(2)}_{x_2x_3,I}\big)\end{aligned} \tag{A23}$$

and

$$\begin{aligned}d_C =& 4 + 10\omega + (4\omega - 12)\big(l_1u_{x_1} + l_2u_{x_2} + l_3u_{x_3}\big)\\ &- 9\omega\big(u^2_{x_1} + u^2_{x_2} + u^2_{x_3}\big) + 6\omega\big(l_1l_2u_{x_1}u_{x_2}\\ &+ l_1l_3u_{x_1}u_{x_3} + l_2l_3u_{x_2}u_{x_3}\big).\end{aligned} \tag{A24}$$

The moments $\rho m^{(2)}_{\alpha\beta}$ are then:

$$\begin{aligned}\rho m^{(2)}_{x_1x_1} =& \tfrac{1}{3}\rho_I\big(10m^{(2)}_{x_1x_1,I} - 2m^{(2)}_{x_2x_2,I} - 2m^{(2)}_{x_3x_3,I}\\ &- 6l_1l_2m^{(2)}_{x_1x_2,I} - 6l_1l_3m^{(2)}_{x_1x_3,I} + 6l_2l_3m^{(2)}_{x_2x_3,I}\big)\\ &+ \tfrac{2}{9}\rho\big(1 - 2l_1u_{x_1} + l_2u_{x_2} + l_3u_{x_3}\big),\end{aligned} \tag{A25}$$

$$\rho m^{(2)}_{x_1x_2} = \tfrac{1}{3}\rho_I\big(-3l_1l_2m^{(2)}_{x_1x_1,I} - 3l_1l_2m^{(2)}_{x_2x_2,I} + 3l_1l_2m^{(2)}_{x_3x_3,I} + 17m^{(2)}_{x_1x_2,I} - l_2l_3m^{(2)}_{x_1x_3,I} - l_1l_3m^{(2)}_{x_2x_3,I}\big) - \tfrac{2}{9}\rho\big(l_1l_2 + l_1u_{x_2} + l_2u_{x_1} + l_1l_2l_3u_{x_3}\big). \quad \text{(A26)}$$

Again, by symmetry, relations for $\rho m^{(2)}_{x_2x_2}$ and $\rho m^{(2)}_{x_3x_3}$ can be obtained directly from $\rho m^{(2)}_{x_1x_1}$, as well as $\rho m^{(2)}_{x_1x_3}$ and $\rho m^{(2)}_{x_2x_3}$ are obtained from $\rho m^{(2)}_{x_1x_2}$. For example, one can get $\rho m^{(2)}_{x_2x_2}$ from Eq. (A25) swapping indexes 1 and 2, leaving 3 alone. For the cross terms, to obtain, for example, the moment $\rho m^{(2)}_{x_1x_3}$, one must swap between indices 1 and 3 in Eq. (A26), leaving aside index 2.

Edges—An edge is defined by the orientations l_1 and l_2. Therefore, $\tilde{\delta}_{l_1} = \tilde{\delta}_{l_2} = 0$ and $\tilde{\delta}_{l_3} = 1$, since $l_3 = 0$. The solution of the linear system at the edges leads to the following relations for the moment ρ:

$$\rho = \rho_I \frac{b_E}{d_E}, \quad \text{(A27)}$$

where

$$b_E = 1656 - 216(\omega - 1)\big[8m^{(2)}_{x_1x_1,I} + 8m^{(2)}_{x_2x_2,I} - 2m^{(2)}_{x_3x_3,I} - 19l_1l_2m^{(2)}_{x_1x_2,I}\big], \quad \text{(A28)}$$

and

$$d_E = 720 - 660\big(l_1u_{x_1} + l_2u_{x_2}\big) + \omega\big(430 - 30\big(l_1u_{x_1} + l_2u_{x_2}\big) + 414l_1l_2u_{x_1}u_{x_2} - 690\big(u^2_{x_1} + u^2_{x_2}\big) - 69u^2_{x_3}\big). \quad \text{(A29)}$$

With a solution for the density ρ, the relations for the moments $\rho m^{(2)}_{\alpha\beta}$ follow:

$$\rho m^{(2)}_{x_1x_1} = \tfrac{1}{23}\rho_I\big(47m^{(2)}_{x_1x_1,I} + m^{(2)}_{x_2x_2,I} - 6m^{(2)}_{x_3x_3,I} + -34l_1l_2m^{(2)}_{x_1x_2,I}\big) - \tfrac{2}{69}\rho\big(-8 + 15l_1u_{x_1} + 8l_2u_{x_2}\big), \quad \text{(A30)}$$

$$\rho m^{(2)}_{x_3x_3} = \tfrac{2}{69}\rho_I\big(-9m^{(2)}_{x_1x_1,I} - 9m^{(2)}_{x_2x_2,I} + 54m^{(2)}_{x_3x_3,I} + 30l_1l_2m^{(2)}_{x_1x_2,I}\big) - \tfrac{4}{69}\rho\big(1 + l_1u_{x_1} + l_2u_{x_2}\big), \quad \text{(A31)}$$

$$\rho m^{(2)}_{x_1x_2} = \tfrac{1}{23}\rho_I\big(l_1l_2\big(-17m^{(2)}_{x_1x_1,I} - 17m^{(2)}_{x_2x_2,I} + 10m^{(2)}_{x_3x_3,I}\big) + 118m^{(2)}_{x_1x_2,I}\big) - \tfrac{19}{69}\rho\big(l_1l_2 + l_1u_{x_2} + l_2u_{x_1}\big), \quad \text{(A32)}$$

$$\rho m^{(2)}_{x_1x_3} = 2\rho_I m^{(2)}_{x_1x_3,I} - \tfrac{1}{3}l_1\rho u_{x_3}. \quad \text{(A33)}$$

Due to symmetry, the relation from $\rho m^{(2)}_{x_2x_2}$ is derived from Eq. (A30) and $\rho m^{(2)}_{x_2x_3}$ is derived from Eq. (A32), simply by exchanging indices 1 and 2 in the previous equations.

Faces—At a given face, we will consider $l_1 \neq 0$ only, so $l_2 = l_3 = 0$, and $\tilde{\delta}_{l_2} = \tilde{\delta}_{l_3} = 1$, $\tilde{\delta}_{l_1} = 0$. The orientation of the face is defined by the sign of l_1. The solution of the linear system for the faces leads to the following relations for the moment ρ:

$$\rho = \rho_I \frac{9(1-\omega)m^{(2)}_{x_1x_1,I} + 12}{\omega\big(1 - 6u^2_{x_1}\big) - 3l_1u_{x_1}(1+\omega) + 9}. \quad \text{(A34)}$$

With the expression for the density ρ, the expressions for the moments $\rho m^{(2)}_{\alpha\beta}$ read:

$$\rho m^{(2)}_{x_1x_1} = \tfrac{3}{2}\rho_I m^{(2)}_{x_1x_1,I} - \tfrac{1}{2}l_1\rho u_{x_1} + \tfrac{1}{6}\rho, \quad \text{(A35)}$$

$$\rho m^{(2)}_{x_2x_2} = \tfrac{4}{33}\rho_I\big(10m^{(2)}_{x_2x_2,I} - m^{(2)}_{x_3x_3,I}\big), \quad \text{(A36)}$$

$$\rho m^{(2)}_{x_1x_2} = 2\rho_I m^{(2)}_{x_1x_2,I} - \tfrac{1}{3}l_1\rho u_{x_2}, \quad \text{(A37)}$$

$$\rho m^{(2)}_{x_2x_3} = \rho_I m^{(2)}_{x_2x_3,I}. \quad \text{(A38)}$$

Due to symmetry, similar expressions for $\rho m^{(2)}_{x_3x_3}$ and $\rho m^{(2)}_{x_1x_3}$ can be obtained from $\rho m^{(2)}_{x_2x_2}$ and $\rho m^{(2)}_{x_1x_2}$, respectively, written down explicitly as:

$$\rho m^{(2)}_{x_3x_3} = \tfrac{4}{33}\rho_I\big(10m^{(2)}_{x_3x_3,I} - m^{(2)}_{x_2x_2,I}\big), \quad \text{(A39)}$$

$$\rho m^{(2)}_{x_1x_3} = 2\rho_I m^{(2)}_{x_1x_3,I} - \tfrac{1}{3}l_1\rho u_{x_3}. \quad \text{(A40)}$$

5. Summary of the boundary conditions

The present boundary condition can be summarized as follows: It is a Dirichlet, onsite explicit scheme, where we have divided the sites as fluid and boundary nodes. Mass is a preserved quantity, while second-order moments are modeled.

The algorithm of the scheme can be described as follows:

(1) In the streaming step, at a given boundary site, record the distribution values propagating or arriving from the neighboring fluid sites (including other boundary sites); the associated microscopic velocity vectors are referred to as the incoming directions.

(2) Compute the second-order moment—the momentum-flux tensor—as a sum over only these incoming distribution values; the distribution values which would arrive from the neighboring solid sites are not considered.

(3) The local velocity is treated as known (due to a Dirichlet boundary condition), whereas the local boundary density still remains unknown.

(4) To ensure mass conservation, the total mass carried by the outgoing postcollisional distribution values (associated with the microscopic velocity vectors opposite to the incoming directions) must be equal to the total mass carried by the incoming precollisional, original distribution values.

(5) The incoming (as well as the outgoing) distribution functions are reconstructed according to the usual regularization procedure. To this end, it is required that the second-order moment, computed as the sum over the reconstructed incoming distributions only, is equal to the moment computed in step 2 (i.e., the sum over the original, incoming distributions).

(6) The conditions from steps 4 and 5 are used to setup a system of equations from which the local density and the

true or full momentum-flux tensor can be solved, ultimately resolving the outgoing reconstructed distributions.

APPENDIX B: BALANCE EQUATION RELATIONS FOR THE TOTAL AND TURBULENT KINETIC ENERGIES

1. Total kinetic energy balance equation

In order to obtain a relation to verify the consistency of the simulation results, let us begin with the total kinetic energy balance equation [39]

$$\partial_t E + \partial_\alpha(u_\alpha E + T_\alpha) = -2\nu S_{\alpha\beta}S_{\alpha\beta}, \tag{B1}$$

where $E = \frac{1}{2}u_\alpha u_\alpha$ is the total kinetic energy, $T_\alpha \equiv u_\alpha p/\rho - 2\nu u_\beta S_{\alpha\beta}$, and $S_{\alpha\beta} = \frac{1}{2}(\partial_\alpha u_\beta + \partial_\beta u_\alpha)$ is the strain tensor, which can be locally computed within the lattice Boltzmann framework through [33,47]

$$S_{\alpha\beta} = \frac{a_s^2}{2\tau}\left(u_\alpha u_\beta - m^{(2)}_{\alpha\beta}\right). \tag{B2}$$

We average Eq. (B1) over the whole volume $\mathcal{V}$ and over time $t \in [t_i, t_f]$ in the statistically stationary state of extension $\delta \equiv t_f - t_i$:

$$\langle\partial_\alpha(u_\alpha E)\rangle_\mathcal{V} + \langle\partial_\alpha T_\alpha\rangle_\mathcal{V} = -2\nu\langle S_{\alpha\beta}S_{\alpha\beta}\rangle_\mathcal{V}, \tag{B3}$$

where usage has been made of the incompressibility condition and, hereafter,

$$\langle\phi\rangle_\mathcal{V} \equiv \frac{1}{\delta}\int_{t_i}^{t_f}\left(\frac{1}{|\mathcal{V}|}\iiint_\mathcal{V}\phi(x,y,z,t)\,dx\,dy\,dz\right)dt$$

and

$$\overline{\phi}(z) \equiv \frac{1}{\delta}\int_{t_i}^{t_f}\left(\frac{1}{L^2}\iint_{L\times L}\phi(x,y,z,t)\,dx\,dy\right)dt$$

for a generic field $\phi = \phi(x,y,z,t)$. Also, $|\mathcal{V}| \equiv L^3$. The time dependence of Eq. (B1) disappears (in the following derivations we will omit, for simplicity, the integration on time, which is, however, implicitly assumed). Applying Gauss theorem to the left-hand side of Eq. (B3) we get:

$$\frac{1}{|\mathcal{V}|}\oiint_{\partial\mathcal{V}}\hat{\boldsymbol{n}}\cdot\boldsymbol{u}E\,d\sigma + \frac{1}{|\mathcal{V}|}\oiint_{\partial\mathcal{V}}\hat{\boldsymbol{n}}\cdot\boldsymbol{T}\,d\sigma = -2\nu\langle S^2\rangle_\mathcal{V}, \tag{B4}$$

where $S^2 \equiv \bar{\bar{S}} : \bar{\bar{S}}$ and the integrals are extended over the bounding surface. The first integral is identically zero because of the impenetrability condition at the walls, $\hat{\boldsymbol{n}}\cdot\boldsymbol{u}|_{\partial\mathcal{V}} = 0$; for the second integral the following holds:

$$\begin{aligned}\oiint_{\partial\mathcal{V}}\hat{\boldsymbol{n}}\cdot\boldsymbol{T}\,d\sigma &= \oiint_{\partial\mathcal{V}}\left(\frac{(\hat{\boldsymbol{n}}\cdot\boldsymbol{u})p}{\rho} - 2\nu(\hat{\boldsymbol{n}}\otimes\boldsymbol{u}) : \bar{\bar{S}}\right)d\sigma \\ &= -2\nu\oiint_{\partial\mathcal{V}}(\hat{\boldsymbol{n}}\otimes\boldsymbol{u}) : \bar{\bar{S}}\,d\sigma,\end{aligned} \tag{B5}$$

again due to $\hat{\boldsymbol{n}}\cdot\boldsymbol{u}|_{\partial\mathcal{V}} = 0$. Because of the no-slip boundary condition, the integrand $(\hat{\boldsymbol{n}}\otimes\boldsymbol{u}) : \bar{\bar{S}}$ is zero over all faces except the lid, where $\boldsymbol{u}(x,y,z=L,t) = (u_L, 0, 0)$. The only nonzero term of $(\hat{\boldsymbol{n}}\otimes\boldsymbol{u}) : \bar{\bar{S}}$ at the lid is $u_x S_{zx}$, hence:

$$\begin{aligned}\oiint_{\partial\mathcal{V}}(\hat{\boldsymbol{n}}\otimes\boldsymbol{u}) : \bar{\bar{S}}\,d\sigma &= \iint_{L\times L}\left(u_x\frac{1}{2}(\partial_x u_z + \partial_z u_x)\right)\Big|_{z=L}dx\,dy \\ &= \iint_{L\times L}\left(u_x\frac{1}{2}(\partial_z u_x)\right)\Big|_{z=L}dx\,dy \\ &= \frac{1}{4}\partial_z\left(\iint_{L\times L}u_x^2\,dx\,dy\right)\Big|_{z=L} \\ &= \frac{L^2}{4}\partial_z\overline{u_x^2}(z)\Big|_{z=L}.\end{aligned} \tag{B6}$$

Combining Eqs. (B4), (B5), and (B6) we get the relation:

$$\langle S^2\rangle_\mathcal{V} = \frac{1}{4L}\partial_z\overline{u_x^2}(z)\big|_{z=L}. \tag{B7}$$

2. Turbulent kinetic energy balance equation

Now we derive a second consistency relation. The balance equation for the turbulent kinetic energy, k, is [39]

$$\partial_t k + U_\alpha\partial_\alpha k + \partial_\alpha T'_\alpha = \mathcal{P} - \epsilon, \tag{B8}$$

where $k \equiv \frac{1}{2}\langle u'_\alpha u'_\alpha\rangle$. The turbulent transport term is

$$T'_\alpha = \tfrac{1}{2}\langle u'_\alpha u'_\beta u'_\beta\rangle + \langle u'_\alpha p'/\rho\rangle - 2\nu\langle u'_\beta s_{\alpha\beta}\rangle,$$

and the production of turbulence is $\mathcal{P} = \langle u'_\alpha u'_\beta\rangle\partial_\beta U_\alpha$. The dissipation of turbulent kinetic energy ϵ is defined by

$$\epsilon = 2\nu s_{\alpha\beta}s_{\alpha\beta},$$

where

$$s_{\alpha\beta} = \tfrac{1}{2}(\partial_\alpha u'_\beta + \partial_\beta u'_\alpha),$$

and the fluctuating velocity $u'_\alpha = u_\alpha - U_\alpha$, where $U_\alpha = \langle u_\alpha\rangle$. Furthermore, $p' = p - \langle p\rangle$. The symbol $\langle ...\rangle$ represents the time average of a property dependent on (x,y,z,t) over a time interval of length δ during which the system is in a statistical steady state:

$$\langle\phi\rangle(x,y,z) \equiv \frac{1}{\delta}\int_{t_i}^{t_f}\phi(x,y,z,t)dt.$$

Taking the average of Eq. (B8) over the volume $\mathcal{V}$ and over time $t \in [t_i, t_f]$, we note that the time-dependent term disappears and we are left with:

$$\langle\partial_\alpha(U_\alpha k)\rangle_\mathcal{V} + \langle\partial_\alpha T'_\alpha\rangle_\mathcal{V} = \langle\mathcal{P}\rangle_\mathcal{V} - \langle\epsilon\rangle_\mathcal{V}. \tag{B9}$$

Following the procedure analogous to the one executed at the total kinetic energy equation, we apply the divergence theorem to the the left-hand side of Eq. (B9). Due to the impenetrability condition, i.e., $\hat{\boldsymbol{n}}\cdot\boldsymbol{U}|_{\partial\mathcal{V}} = 0$, the term $\langle\partial_\alpha(U_\alpha k)\rangle_\mathcal{V}$ is identically zero. For the second term at the left-hand side of Eq. (B9) we have

$$\begin{aligned}\oiint_{\partial\mathcal{V}}\hat{\boldsymbol{n}}\cdot\boldsymbol{T}'d\sigma = \oiint_{\partial\mathcal{V}}\Bigg(&\frac{1}{2}\hat{\boldsymbol{n}}\cdot\boldsymbol{u}'u'^2 + \frac{(\hat{\boldsymbol{n}}\cdot\boldsymbol{u}')p'}{\rho} \\ &- 2\nu(\hat{\boldsymbol{n}}\otimes\boldsymbol{u}') : \bar{\bar{s}}\Bigg)d\sigma = 0,\end{aligned} \tag{B10}$$

since the velocity fluctuation at the boundaries is null, i.e., $\boldsymbol{u}'|_{\partial\mathcal{V}} = (0, 0, 0)$. Then, the relation between production and dissipation follows:

$$\langle \mathcal{P} \rangle_{\mathcal{V}} = \langle \epsilon \rangle_{\mathcal{V}}.$$

APPENDIX C: SIMULATION CODE

The regularized boundary conditions were implemented in HARVEY, a parallelized hemodynamics code [18]. The code is written in `C` and `C++` and uses `MPI` for parallelization. As can be seen in Algorithm 1, the regularized wall boundary condition occurs after both the collision and stream steps.

As most of the operations in the boundary condition are constant across time steps, the values are cached in a lookup table. The appropriate value is then indexed using the type of wet wall condition (face, edge, or corner).

Algorithm 1 Regularized lattice Boltzmann for lid-driven cavity

procedure LBM *ts* ▷ ts is the total number of time steps in the simulation
  $d \leftarrow$ initialize_distribution() ▷ Maxwellian equilibrium distribution
  $i = 0$
  while $i < ts$ **do**
    $d \leftarrow$ collide(d)
    $d \leftarrow$ stream(d)
    $w \leftarrow$ filter_wall_sites(d)
    $m_I \leftarrow$ incoming_moments(w) ▷ Moments using only the incoming site D3Q19 velocities for a given wall type
    $m_R \leftarrow$ WALL_CONDITION(m_I) ▷ All moments after wall condition is applied
    $w \leftarrow$ convert_to_discrete_velocities(m_R)
    $d \leftarrow$ update_wall_sites(d, w)
  end while
  $p \leftarrow$ get_density(d)
  $v \leftarrow$ get_velocity(d)
  return p, v
end procedure
procedure WALL_CONDITION (m_I)
  $\rho_I \leftarrow$ get_rho(m_I)
  $m_{xx_I} \leftarrow$ get_secondmoments(m_I)
  $\rho \leftarrow$ density_at_wall(ρ_I, m_{xx_I}) ▷ Use Eq. (A22) for a corner, (A27) for an edge, and (A34) for a face
  $m_{xx} \leftarrow$ density_at_wall(m_{xx_I}, ρ_I, ρ) ▷ Use Eqs. (A25) and (A26) for a corner, (A30)–(A33) for an edge, and (A35)–(A40) for a face
  $m_x \leftarrow 0$ ▷ First-order moment, no slip condition
  $m_R \leftarrow$ pack_moments(ρ, m_x, m_{xx})
  return m_R
end procedure

[1] L. D. Landau and E. M. Lifshitz, *Fluid Mechanics: Landau and Lifshitz: Course of Theoretical Physics*, 2nd ed., Vol. 6 (Butterworth-Heinemann, London, 1987).

[2] H. Chen, S. Kandasamy, S. Orszag, R. Shock, S. Succi, and V. Yakhot, Science **301**, 633 (2003).

[3] D. N. Ku, Annu. Rev. Fluid Mech. **29**, 399 (1997).

[4] M. D. de Tullio, A. Cristallo, E. Balaras, and R. Verzicco, J. Fluid Mech. **622**, 259 (2009).

[5] D. Zumbrunnen, K. Miles, and Y. Liu, Composites, Part A **27**, 37 (1996).

[6] P. Shankar and M. Deshpande, Annu. Rev. Fluid Mech. **32**, 93 (2000).

[7] K. M. Tse, P. Chiu, H. P. Lee, and P. Ho, J. Biomech. **44**, 827 (2011).

[8] A. K. Prasad and J. R. Koseff, Phys. Fluids A **1**, 208 (1989).

[9] S. Albensoeder and H. C. Kuhlmann, J. Comput. Phys. **206**, 536 (2005).

[10] E. Leriche, J. Sci. Comput. **27**, 335 (2006).

[11] R. Bouffanais, M. O. Deville, and E. Leriche, Phys. Fluids **19**, 055108 (2007).

[12] D. A. Shetty, T. C. Fisher, A. R. Chunekar, and S. H. Frankel, J. Comput. Phys. **229**, 8802 (2010).

[13] K. N. Premnath, M. J. Pattison, and S. Banerjee, Phys. Rev. E **79**, 026703 (2009).

[14] K. Anupindi, W. Lai, and S. Frankel, Comput. Fluids **92**, 7 (2014).

[15] M. Bouzidi, M. Firdaouss, and P. Lallemand, Phys. Fluids **13**, 3452 (2001).

[16] D. d'Humières, Philos. Trans. R. Soc. Lond. A **360**, 437 (2002).
[17] A. Montessori, G. Falcucci, P. Prestininzi, M. La Rocca, and S. Succi, Phys. Rev. E **89**, 053317 (2014).
[18] A. Randles, E. W. Draeger, T. Oppelstrup, L. Krauss, and J. A. Gunnels, in *Proceedings of the International Conference for High Performance Computing, Networking, Storage and Analysis (SC '15)* (ACM, New York, NY, 2015).
[19] U. Frisch, B. Hasslacher, and Y. Pomeau, Phys. Rev. Lett. **56**, 1505 (1986).
[20] G. R. McNamara and G. Zanetti, Phys. Rev. Lett. **61**, 2332 (1988).
[21] F. J. Higuera, S. Succi, and R. Benzi, Europhys. Lett. **9**, 345 (1989).
[22] Y. Qian, D. d'Humières, and P. Lallemand, Europhys. Lett. **17**, 479 (1992).
[23] S. Succi, *The Lattice Boltzmann Equation: For Fluid Dynamics and Beyond* (Oxford University Press, Oxford, 2001).
[24] A. J. C. Ladd, J. Fluid Mech. **271**, 285 (1994).
[25] J. Latt and B. Chopard, Math. Comput. Simul. **72**, 165 (2006).
[26] H. Grad, Commun. Pure Appl. Math. **2**, 325 (1949).
[27] K. K. Mattila, L. A. Hegele, Jr., and P. C. Philippi, Phys. Rev. E **91**, 063010 (2015).
[28] Q. Zou and X. He, Phys. Fluids **9**, 1591 (1997).
[29] T. Inamuro, M. Yoshino, and F. Ogino, Phys. Fluids **7**, 2928 (1995).
[30] S. Ansumali and I. V. Karlin, Phys. Rev. E **66**, 026311 (2002).
[31] T. Reis and P. J. Dellar, Phys. Fluids **24**, 112001 (2012).
[32] S. Bennett, P. Asinari, and P. J. Dellar, Int. J. Numer. Methods Fluids **69**, 171 (2012).
[33] J. Latt, B. Chopard, O. Malaspinas, M. Deville, and A. Michler, Phys. Rev. E **77**, 056703 (2008).
[34] B. Dorschner, S. Chikatamarla, F. Bösch, and I. Karlin, J. Comput. Phys. **295**, 340 (2015).
[35] S. Krithivasan, S. Wahal, and S. Ansumali, Phys. Rev. E **89**, 033313 (2014).
[36] O. Malaspinas, B. Chopard, and J. Latt, Comput. Fluids **49**, 29 (2011).
[37] P. A. Skordos, Phys. Rev. E **48**, 4823 (1993).
[38] Z. Guo, C. Zheng, and B. Shi, Phys. Fluids **14**, 2007 (2002).
[39] S. B. Pope, *Turbulent Flows* (Cambridge University Press, Cambridge, 2000).
[40] L. Biferale, F. Mantovani, M. Sbragaglia, A. Scagliarini, F. Toschi, and R. Tripiccione, Phys. Fluids **22**, 115112 (2010).
[41] T. Krüger, H. Kusumaatmaja, A. Kuzmin, O. Shardt, G. Silva, and E. M. Viggen, *The Lattice Boltzmann Method* (Springer, Berlin, 2017).
[42] P. C. Philippi, L. A. Hegele, Jr., L. O. E. dos Santos, and R. Surmas, Phys. Rev. E **73**, 056702 (2006).
[43] S. S. Chikatamarla, S. Ansumali, and I. V. Karlin, Phys. Rev. Lett. **97**, 010201 (2006).
[44] M. Atif, P. K. Kolluru, C. Thantanapally, and S. Ansumali, Phys. Rev. Lett. **119**, 240602 (2017).
[45] K. K. Mattila, P. C. Philippi, and L. A. Hegele, Jr., Phys. Fluids **29**, 046103 (2017).
[46] C. Coreixas, G. Wissocq, G. Puigt, J.-F. Boussuge, and P. Sagaut, Phys. Rev. E **96**, 033306 (2017).
[47] S. Hou, J. Sterling, S. Chen, and G. Doolen, Fields Inst. Commun. **6**, 151 (1996).